J. Appl. Comput. Mech., xx(x) (2026) 1-13
DOI: 10.22055/jacm.2026.49819.6267

ISSN: 2383-4536
jacm.scu.ac.ir

Shahid Chamran University of Ahvaz

Journal of Applied and Computational Mechanics



Research Paper

Hot Deformation Behavior and Processing Map Development for Biodegradable Mg–1Zn–0.2Ca Alloy

M. Kamrava[1], A. Najafi[1], Y. Mazaheri[1], E. Bagherpour[2], M. Reihanian[3], R.Z. Valiev[4], R. Ebrahimi[1]

[1] Department of Materials Science and Engineering, School of Engineering, Shiraz University, Shiraz, Iran

[2] Brunel Centre for Advanced Solidification Technology (BCAST), Brunel University of London, Uxbridge, UB8 3PH, UK

[3] Department of Materials Science and Engineering, Faculty of Engineering, Shahid Chamran University of Ahvaz, Ahvaz, Iran

[4] Institute of Physics of Advanced Materials, Ufa University of Science and Technology, Ufa, 450076, Russia

Received September 17 2026; Revised October 09 2026; Accepted for publication October 11 2026.
✉ Corresponding author: R. Ebrahimi (ebrahimy@shirazu.ac.ir)
© 2026 Published by Shahid Chamran University of Ahvaz

Abstract. The hot deformation behavior and workability of an extruded biodegradable Mg–1Zn–0.2Ca alloy (initial grain size 25.7 μm) were investigated by isothermal compression at temperatures of 200–400 °C and strain rates of 0.001–1 s^{-1}. The flow stress decreased with increasing temperature and increased with increasing strain rate, and pronounced late-stage stress losses at low temperatures were associated, at least partly, with specimen cracking. Processing maps were developed at true strains of 0.3, 0.5, and 0.7 using the dynamic materials model, with the unstable domain defined as the union of the regions predicted by two flow-instability criteria for a conservative assessment. At a true strain of 0.7, the power dissipation efficiency reached a maximum of about 0.46 at approximately 360–370 °C and 0.005–0.01 s^{-1}, and a broader stable domain was identified at approximately 340–380 °C and 0.001–0.1 s^{-1}. The maps evolved non-monotonically with strain. Cracking occurred at all strain rates at 200 °C, at 0.1–1 s^{-1} at 240 °C, and at 1 s^{-1} at 280 °C, but not at 320–400 °C. Optical microscopy showed that the crack at 200 °C followed an inclined path of localized deformation, that a fine, uniform microstructure formed at the efficiency maximum, and that localized deformation bands developed without cracking at 360 °C and 1 s^{-1}, where instability was predicted. The results establish a hot-working window for the extruded alloy, based on single tests per condition, and provide guidance for optimizing its thermomechanical processing.

Keywords: Mg–Zn–Ca alloy; Hot deformation; Processing map; Deformation instability; Cracking.

1. Introduction

Magnesium alloys are promising biodegradable materials for temporary orthopedic implants because their bone-like density and elastic modulus can reduce stress shielding, while their gradual degradation can eliminate the need for implant removal after healing [1-3]. Among them, Mg–Zn–Ca alloys are particularly attractive because Zn and Ca are biologically relevant elements that can improve the mechanical performance of magnesium through strengthening, grain refinement, and texture modification [3-6]. However, their performance and reliability depend strongly on composition, microstructure, and processing history. Recent studies have demonstrated the susceptibility of magnesium alloys to deformation-induced damage and fracture under unfavorable loading and processing conditions, highlighting the importance of understanding how processing conditions influence deformation stability and cracking [7-9]. Because processing history strongly affects microstructure and, consequently, deformation and failure behavior, thermomechanical processing provides an important means of controlling the performance of Mg–Zn–Ca alloys. In particular, hot deformation can activate additional slip systems and promote dynamic recovery and recrystallization, thereby refining the microstructure and modifying texture [10-12]. The hot deformation behavior and the susceptibility to instability and cracking are therefore governed by the interplay among deformation temperature, strain rate, accumulated strain, and microstructural evolution.

Several studies have investigated the thermomechanical behavior of Mg–Zn–Ca alloys, demonstrating that their microstructure and hot workability are strongly influenced by alloy composition, deformation conditions, and processing history. A comprehensive review by Rao et al. [13] showed that Ca-containing Mg alloys generally exhibit limited hot workability and require carefully selected combinations of temperature and strain rate to promote dynamic recrystallization (DRX), with processing maps providing an effective means of identifying suitable hot-working conditions. The review further highlighted that flow instability is most likely to occur at low temperatures and high strain rates, particularly in alloys with higher Ca contents because intermetallic particles suppress DRX. In a subsequent study, Rao et al. [14] employed processing maps to evaluate the hot workability of as-cast Mg–1Zn–1Ca (ZX11) alloy and identified two DRX-dominated processing domains over the temperature range of approximately 280–400 °C

Published online: October 23 2026

and strain rates between 0.0003 and 0.1 s^{-1}. They also demonstrated that the dominant deformation mechanism changed from basal slip to prismatic slip with increasing temperature and identified flow instability regions associated with adiabatic shear banding, flow localization, and grain-boundary cracking under unfavorable deformation conditions.

Experimental studies have confirmed these observations. Hradilova et al. [15] demonstrated that Ca addition promotes DRX during hot deformation of Mg–Zn alloys by controlling DRX grain growth through precipitation pinning, resulting in a finer and more homogeneous microstructure. Papillon et al. [16] investigated the hot compressive behavior of Mg–Ca(–Zn) alloys and reported that DRX is strongly dependent on deformation conditions and alloy composition, enabling the identification of optimum processing parameters for safe hot deformation. Zareian et al. [17] showed that Ca addition combined with hot extrusion significantly refines the grain structure, fragments second-phase particles, and improves the mechanical properties of Mg–Zn alloys, although excessive Ca additions lead to extrusion defects and reduced ductility. More recently, Zheng et al. [18] reported that nano-MgO additions promote DRX, increase the power dissipation efficiency, reduce instability regions in processing maps, and improve the hot workability of Mg–3Zn–0.2Ca alloys.

For the Mg–1Zn–0.2Ca alloy specifically, Najafi et al. [19] showed that hot extrusion through a cosine-profile die produced significant grain refinement, texture evolution, and heterogeneous recrystallization, while Razavi et al. [20] modeled static recrystallization during non-isothermal heating of the severely deformed alloy. More recently, Mirabdolazimi et al. [21] investigated the thermal stability and annealing-induced hardening behavior of ultrafine-grained Mg–1Zn–0.2Ca processed by high-pressure torsion. Collectively, these studies demonstrate the strong influence of thermomechanical processing on the microstructural evolution and mechanical behavior of Mg–Zn–Ca alloys. However, despite these advances, systematic studies on the hot workability and processing-map-based optimization of extruded Mg–1Zn–0.2Ca alloy remain very limited, particularly regarding the evolution of processing maps over a wide range of deformation temperatures, strain rates, and accumulated strains.

Processing maps based on the dynamic materials model (DMM) provide an effective framework for evaluating the hot workability of metallic materials. By combining the efficiency of power dissipation with instability criteria, the DMM identifies deformation domains associated with stable plastic flow as well as regions susceptible to flow localization and cracking [22, 23]. Nevertheless, the predictive capability of processing maps depends on the reliability of the flow stress data and the numerical procedures used in their construction. Moreover, factors such as friction, barreling, thermal gradients, and deformation heating may influence the measured flow behavior during hot compression, potentially affecting the predicted processing windows [24, 25]. Therefore, processing-map predictions should be validated through complementary experimental observations, including the macroscopic characteristics of the deformed specimens and, where available, microstructural evidence.

The present study systematically investigates the hot deformation behavior and strain-dependent hot workability of an extruded Mg–1Zn–0.2Ca alloy by isothermal compression testing over a wide range of deformation temperatures (200–400 °C) and strain rates (0.001–1 s^{-1}). Unlike previous studies, which have primarily focused on microstructural evolution or mechanical properties under specific processing conditions, the present work establishes processing maps at true strains of 0.3, 0.5, and 0.7 using the dynamic materials model and evaluates flow stability using two complementary instability criteria. The predicted processing windows are further assessed by comparison with the macroscopic response of the compressed specimens to correlate the processing-map predictions with the experimentally observed deformation behavior. The results provide a comprehensive assessment of the evolution of hot workability with accumulated strain, establish a practical processing window for extruded Mg–1Zn–0.2Ca alloy, and provide guidance for the design and optimization of subsequent thermomechanical processing routes for this biodegradable magnesium alloy.

2. Materials and Methods

2.1. Alloy processing

As-received extruded Mg–1Zn–0.2Ca alloy bars with a diameter of 15 mm and the chemical composition given in Table 1 were used in this study. The bars had been produced by homogenization of the as-cast alloy at 450 °C for 8 h, followed by extrusion at 400 °C with an extrusion ratio of 100:1 and a ram speed of 14 mm/min (average strain rate of about 0.04 s^{-1}). The initial microstructure of the extruded alloy, observed on the plane normal to the extrusion direction, is shown in Fig. 1. It consists mainly of equiaxed polygonal grains with well-defined boundaries and an average grain size of 25.7 μm. The microstructure is not fully uniform: regions of larger equiaxed grains coexist with regions of finer, darker-etching features, and fine parallel lines are visible inside some grains. No continuous network of coarse second-phase particles was resolved by optical microscopy; the distribution of the Ca-containing second phases was not characterized in the present work.

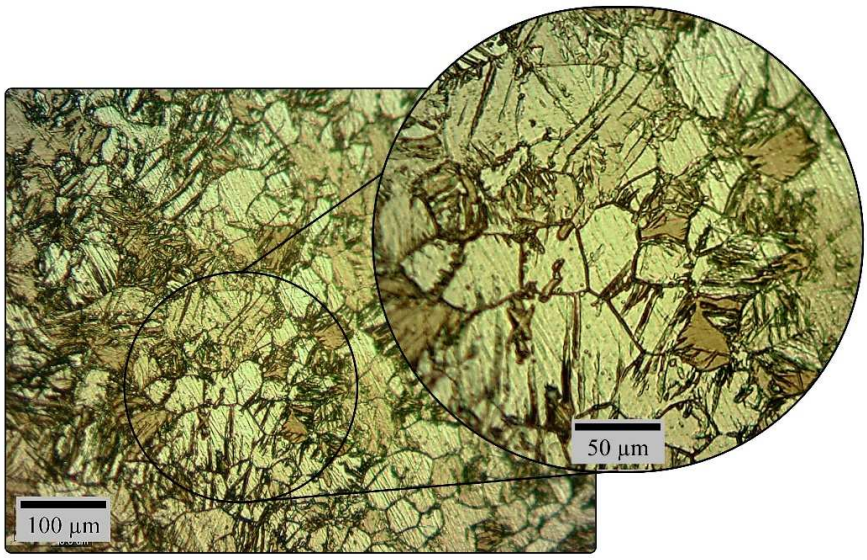


Fig. 1. Optical microstructure of the as-extruded Mg–1Zn–0.2Ca alloy, observed on the plane normal to the extrusion direction. The inset shows a higher-magnification view of the circled area.

Table 1. The chemical composition of the Mg–1Zn–0.2Ca alloy, (wt.%).

Si	Zn	Al	Be	Ca	Fe	Pd	Mg
0.05	1	0.04	0.001	0.21	0.003	0.013	Bal.

2.2. Isothermal compression testing

Cylindrical compression specimens, 12 mm in diameter and 18 mm in height, were machined from the extruded material. The longitudinal axis of each specimen was parallel to the extrusion direction. The specimen end faces were ground using progressively finer abrasive papers to remove surface oxides and machining marks and to improve surface finish and parallelism. The test matrix comprised six deformation temperatures (200, 240, 280, 320, 360 and 400 °C) and four nominal strain rates (0.001, 0.01, 0.1 and 1 s^{-1}) giving a total of 24 temperature–strain rate combinations.

Before testing, J-type thermocouples were attached to the mid-height surface of each specimen to measure and control the specimen temperature. Friction at the specimen–anvil interfaces was reduced using graphite foil and a nickel-based anti-seize compound, Gasoila THRED GARD. The same interface arrangement was used at both ends of the specimen. The specimens were resistance heated at 5 °C s^{-1} to the selected deformation temperature under a vacuum of approximately 4×10^{-4} Torr. They were then held at the test temperature for 120 s to allow the temperature to stabilize throughout the specimen. Compression was applied at a constant nominal strain rate to a final true strain of 0.7. Because all tests were terminated at the same final true strain, the nominal height reduction was identical for all conditions; differences in specimen appearance therefore reflect the homogeneity of deformation (barreling, shear localization and cracking) rather than the total strain imposed. Immediately after deformation, the specimens were cooled using a pressurized air jet at an average cooling rate of approximately 20 °C s^{-1}. The cooling rate was determined from the temperature–time data recorded by the thermocouple during cooling.

Compression tests were performed on a Gleeble 3800 thermomechanical simulator equipped with the Hydrawedge system, which provides controlled strain and strain-rate histories. Preliminary and calibration tests were performed before the main test matrix to establish the testing procedure. During every test, the specimen temperature, force, displacement/strain and strain rate were continuously recorded. After each test, the recorded histories were checked to confirm that the prescribed conditions had been achieved. A test showing an experimental abnormality or unacceptable deviation was rejected and repeated using a new specimen. The dataset therefore contains one successfully completed and validated test for each of the 24 temperature-strain-rate conditions. Systematic replicate testing was not performed for every condition, because of the limited availability of the Gleeble system, the long duration of the low-strain-rate tests and the limited amount of extruded material. Specimen-to-specimen scatter could therefore not be quantified, and error bars are not provided.

The true stress–true strain data were not corrected for friction or deformation heating. Friction was reduced by graphite foil and a nickel-based anti-seize compound, and limited barreling was observed. These two effects act in opposite directions: friction and barreling increase the measured flow stress, whereas deformation heating raises the specimen temperature and lowers it. Both are most pronounced at high strain rates, so they partly compensate each other, although the compensation was not quantified. An upper-bound adiabatic estimate suggests a temperature rise of up to about 20–50 K at 1 s^{-1}, negligible at 0.001 s^{-1}. Since the maps depend mainly on the variation of stress with strain rate, the main trends are expected to be less affected than the absolute stress values, but quantitative boundaries, particularly at 1 s^{-1}, should be treated with caution.

2.3. Microstructural characterization

For microstructural examination, the initial extruded material was sectioned normal to the extrusion direction, and the deformed specimens were sectioned parallel to the compression axis through the center. The specimens were prepared by conventional metallographic procedures, consisting of successive grinding and mechanical polishing, and then etched with a modified picral solution (6.5 mL acetic acid, 3.5 g picric acid, 20 mL distilled water and 100 mL ethanol). The microstructures were examined using a Leitz optical microscope.

3. Results and Discussion

3.1. Flow characteristics and deformation mechanisms

Figure 2 shows the true stress–true strain curves of the extruded Mg–1Zn–0.2Ca alloy tested at temperatures between 200 and 400 °C and strain rates of 0.001–1 s^{-1}. Under most conditions, the flow stress rises rapidly during the early stage of deformation, reaches a maximum, and then decreases progressively or approaches a near-steady value. The initial increase is associated with work hardening and dislocation accumulation [26], while the subsequent response indicates an increasing contribution from thermally activated restoration processes, namely dynamic recovery (DRV) and dynamic recrystallization (DRX). Abrupt stress drops associated with specimen damage, however, should not be misinterpreted as intrinsic flow softening. Similar flow behavior, with an initial hardening stage followed by progressive softening, has been widely reported for hot-deformed alloys, where the softening has been attributed to the combined action of DRV, DRX and, depending on the alloy and deformation conditions, other restoration processes [27-29]. In particular, progressive flow softening during DRX has been linked to the continuous nucleation and growth of recrystallized grains, which gradually replace the work-hardened microstructure [28].

The alloy exhibits positive strain rate sensitivity over the investigated temperature range. At each temperature, increasing the strain rate ($\dot{\varepsilon}$) generally increases both the peak stress and the subsequent flow stress level. For example, at 200 °C, the peak stress increases from approximately 105 MPa at 0.001 s^{-1} to nearly 200 MPa at 1 s^{-1}. A similar ordering is maintained at higher temperatures, although the differences between the curves diminish as the temperature increases. At high strain rates, deformation is imposed more rapidly than time-dependent dislocation rearrangement and restoration can occur, leading to greater dislocation accumulation and higher deformation resistance. Lower strain rates provide more time for these processes, thereby producing lower flow stresses. This dependence of the flow stress on strain rate is consistent with the competition between strain hardening and thermally activated restoration reported for other hot-deformed alloys, in which a higher strain rate shortens the time available for restoration and increases the flow stress, while a lower strain rate allows greater restoration [27, 28].

Temperature also has a pronounced effect on the deformation response. At a given strain rate, both the peak stress and the subsequent flow stress decrease as the temperature increases. At 1 s^{-1}, for instance, the peak stress falls from approximately 200 MPa at 200 °C to about 60 MPa at 400 °C. This reduction reflects the increasing ease of thermally activated dislocation motion and restoration at elevated temperatures. DRV and DRX play critical roles in the post-peak response; typically, DRV acts as the primary restoration mechanism, while DRX becomes increasingly active at higher temperatures and lower strain rates, promoting more continuous and smooth flow softening.

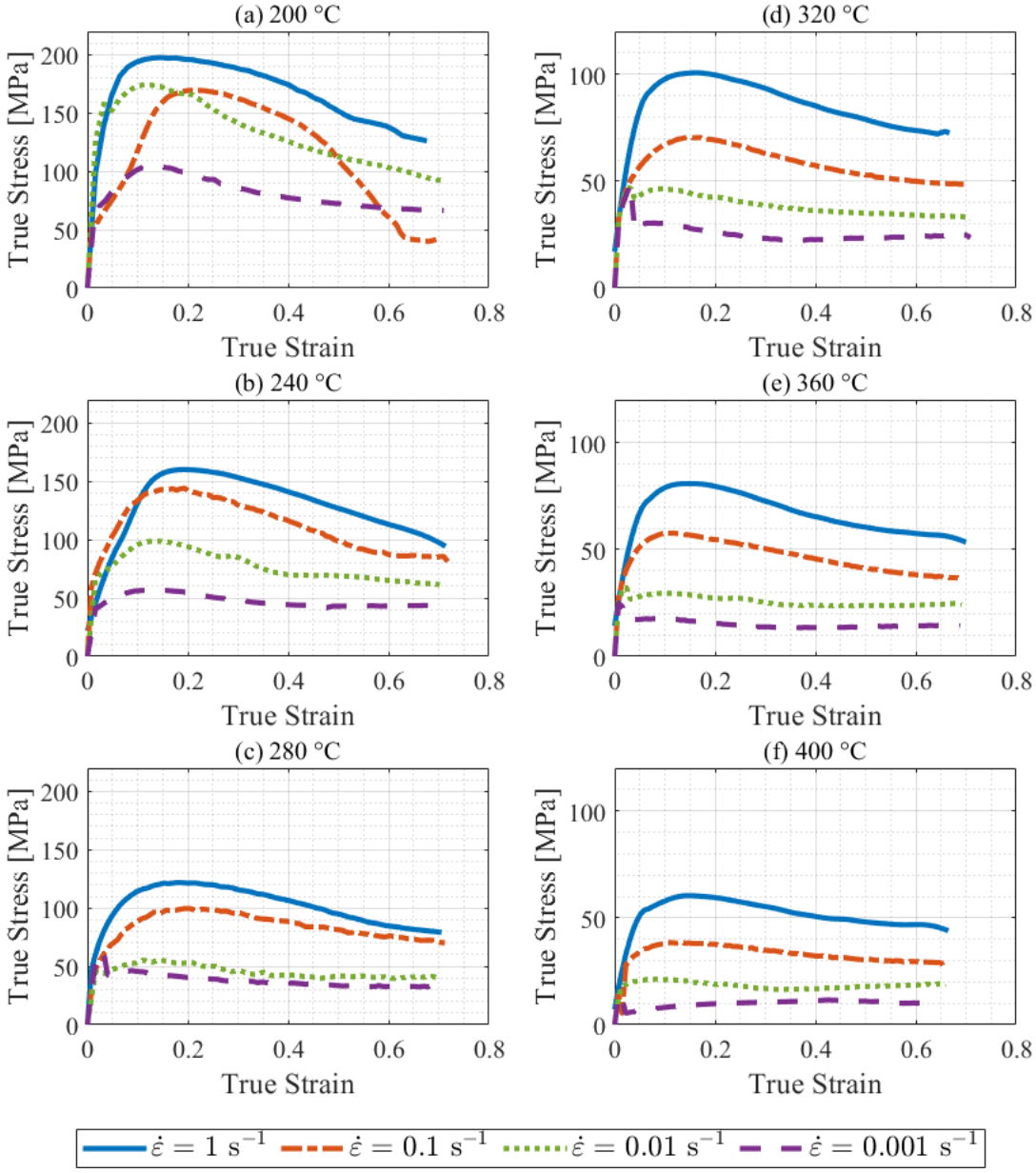


Fig. 2. True stress–true strain curves of the extruded Mg–1Zn–0.2Ca alloy obtained at temperatures of 200–400 °C and strain rates of 0.001, 0.01, 0.1 and 1 s^{-1}.

The role of microstructural features in this process may also be significant. In multiphase alloys, interfaces and second phases can impede dislocation glide and promote recrystallization, but this effect is not constant, because the interfaces themselves evolve during deformation [27]. By analogy, the Ca-containing second-phase particles in the present alloy may influence local dislocation accumulation and recrystallization, and their effect may change as deformation proceeds. This possibility requires confirmation by microstructural examination.

The least stable response is observed at 200 °C and 0.1 s^{-1} (and to some extent at 0.01 s^{-1}). Under the 0.1 s^{-1} condition, the stress reaches a peak of approximately 170 MPa at a true strain of about 0.25 and then decreases gradually before falling sharply beyond a strain of approximately 0.5. The corresponding physical specimen shows macroscopic damage, indicating that the final stress drop is largely associated with cracking and a loss of effective load-bearing area rather than intrinsic softening alone. The curve obtained at 0.01 s^{-1} also shows substantial post-peak softening, which should likewise be interpreted alongside the visual appearance of the deformed specimen.

At 240 °C and 280 °C, the peak stresses are lower than those measured at 200 °C, and the post-peak decrease is generally smoother. At 320–400 °C, the curves show markedly lower stress levels and more gradual softening after the peak. This behavior suggests that enhanced thermal restoration increasingly offsets work hardening as the temperature rises. The relatively smooth flow response at these temperatures is consistent with improved hot deformability, although processing map and specimen damage analyses are still required to assess flow stability definitively. Some anomalous fluctuations are visible in individual low-strain-rate curves. In particular, the 0.001 s^{-1} curve at 280 °C shows a local decrease and recovery in stress at intermediate strains. This feature may reflect control fluctuations, signal noise, or changes in friction during the long-duration test, rather than a specific deformation mechanism.

The flow curves demonstrate that the deformation response of the extruded Mg–1Zn–0.2Ca alloy is strongly controlled by temperature and strain rate. Increasing the temperature lowers deformation resistance, whereas increasing the strain rate raises the flow stress. Low-temperature deformation also produces a greater tendency toward severe post-peak stress loss and specimen damage. These results provide the experimental foundation for the subsequent processing map analysis.

3.2. Processing map analysis

The hot workability of the Mg–1Zn–0.2Ca alloy was evaluated using processing maps based on the dynamic materials model (DMM). At true strains of 0.3, 0.5 and 0.7, the flow stress was extracted from each true stress–true strain curve at the corresponding deformation temperature and strain rate. In the DMM, the deforming workpiece is treated as a nonlinear dissipator of power. At a given temperature and strain, the instantaneous power input per unit volume, p, is divided into the dissipator content, G, and the dissipator co-content, J [22, 23]:

$$p = \sigma.\dot{\varepsilon} = G + J = \int_0^{\dot{\varepsilon}} \sigma.d\dot{\varepsilon} + \int_0^{\sigma} \dot{\varepsilon}.d\sigma \tag{1}$$

where σ is the flow stress and $\dot{\varepsilon}$ is the strain rate. The G term represents the power dissipated mainly through plastic deformation and the associated heat generation, whereas J is the complementary portion associated with changes in the material state during deformation. These changes may include dynamic recovery, dynamic recrystallization and other microstructural processes; however, the active mechanism cannot be identified from a processing map alone. The partitioning of power between G and J is governed by the strain rate sensitivity parameter, m, defined as [22, 23]:

$$m = \left(\frac{\partial \ln\sigma}{\partial \ln\dot{\varepsilon}}\right) \tag{2}$$

At each selected strain and temperature, the relationship between ln σ and ln $\dot{\varepsilon}$ was fitted using polynomial regression. The local slope of the fitted relationship was used to determine m, after which η was calculated across the investigated temperature–strain rate domain.

The relationship between ln σ and ln $\dot{\varepsilon}$ was fitted at each temperature and strain using a third-order polynomial:

$$\ln\sigma = a + b(\ln\dot{\varepsilon}) + c(\ln\dot{\varepsilon})^2 + d(\ln\dot{\varepsilon})^3 \tag{3}$$

The strain-rate sensitivity was then obtained from the derivative of this fit:

$$m = \left(\frac{\partial \ln\sigma}{\partial \ln\dot{\varepsilon}}\right) = b + 2c(\ln\dot{\varepsilon}) + 3d(\ln\dot{\varepsilon})^2 \tag{4}$$

The strain rate sensitivity was evaluated at each true strain used for the processing maps. Because the fit uses four strain rates, the cubic polynomial is exactly determined, and m, being a derivative, is most sensitive to fitting error at the ends of the strain-rate range. m and the quantities derived from it are therefore interpreted through trends across neighboring conditions, not through individual values.

The strain-rate sensitivity m is the quantity from which η and both instability criteria are derived, so its variation is reflected directly in the processing maps. A higher m increases the resistance to localized flow, whereas a low m promotes localization and cracking. Accordingly, m is highest within the high-efficiency domain at about 360 °C and low-to-intermediate strain rates, and it is moderate and positive over most of the crack-free region at 320–400 °C. At 240 and 280 °C, m decreases at the highest strain rate, consistent with the reduced stability and cracking at these conditions. At 200 °C, m varies erratically with strain rate and is low at intermediate strain rates, which indicates a tendency toward flow localization and agrees with the cracking observed at this temperature. The high value obtained at 200 °C and 1 s^{-1} lies at the end of the fitted strain-rate range, where the polynomial derivative is least reliable, and the specimen cracked under this condition. It likely reflects the fitting behavior and not a favorable deformation response.

3.2.1. *Power dissipation efficiency (η)*

The efficiency of power dissipation, η, describes the fraction of the power input associated with changes in the material state relative to the maximum dissipator co-content. Several approaches have been proposed for power dissipation parameter [30]. In the present study, η was evaluated using the integral formulation reported by Ebrahimi and Najafizadeh [31]:

$$\eta = \frac{\frac{m\dot{\varepsilon}_{min}^{m+1}}{m+1} + \int_{\dot{\varepsilon}_{min}}^{\dot{\varepsilon}} m\dot{\varepsilon}^m.d\dot{\varepsilon}}{\frac{\dot{\varepsilon}^{m+1}}{2}} \tag{5}$$

where $\dot{\varepsilon}_{min}$ is the lower bound of the investigated strain rate interval. This formulation allows the variation of m with strain rate to be considered rather than assuming a single constant value over the full strain rate range.

Figure 3 presents the power dissipation efficiency map of the extruded Mg–1Zn–0.2Ca alloy at a true strain of 0.7. The efficiency parameter, η, varies markedly with both deformation temperature and strain rate. In general, the highest values occur at elevated temperatures and low to intermediate strain rates, whereas lower efficiencies are found over much of the low-temperature region. A high-efficiency domain is centered at approximately 340–380 °C and strain rates between about 0.001 and 0.1 s^{-1}, where η reaches approximately 0.4–0.46. This indicates that, within the DMM framework, a relatively large fraction of the deformation power is associated with microstructural changes rather than plastic dissipation alone. The location of this domain is consistent with the lower flow stresses and smoother post peak response observed at elevated temperatures. However, the active restoration mechanism cannot be identified from the efficiency map alone. Confirmation of dynamic recovery, dynamic recrystallisation or grain refinement would require supporting microstructural evidence.

At intermediate temperatures, approximately 260–320 °C, and strain rates broadly between 0.01 and 0.1 s^{-1}, η is typically in the range of 0.25–0.30. This region therefore represents a moderate efficiency domain between the low temperature and high temperature responses. The corresponding flow curves show lower deformation resistance than those obtained at 200–240 °C, but the efficiency remains below that of the high temperature domain. This may reflect a less extensive contribution from thermally activated restoration processes, although no specific mechanism can be assigned without microstructural characterization.

Most of the region below approximately 240 °C is characterized by relatively low η, particularly at low to intermediate strain rates. The lower efficiency is consistent with the greater deformation resistance and the increased tendency towards cracking observed at these temperatures. Restricted non-basal slip activity and limited atomic mobility may contribute to this behavior, but the interpretation should also account for the influence of damage on the measured flow stress data.

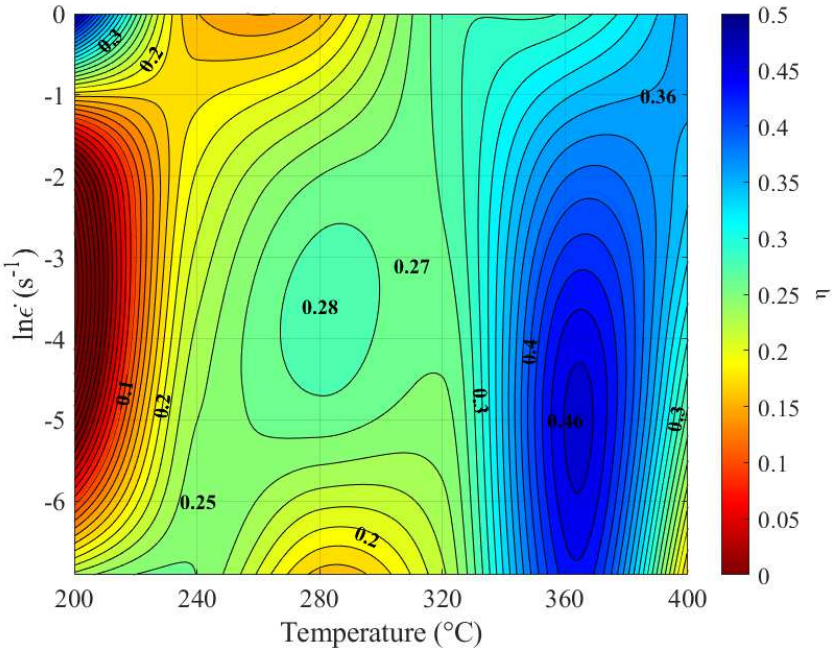


Fig. 3. Power dissipation efficiency map of the extruded Mg–1Zn–0.2Ca alloy at a true strain of 0.7. The strain rate axis is expressed as $ln\,\dot{\varepsilon}$, where $\dot{\varepsilon}$ is strain rate.

A narrow region of comparatively high efficiency appears near 200–220 °C and strain rates approaching 1 s^{-1}. This region cannot be regarded as a favorable processing domain on the basis of η alone. It lies close to the boundaries of the experimental temperature and strain rate ranges, where numerical differentiation and contour interpolation are particularly sensitive to the fitting procedure. In addition, the specimens deformed at 200 °C showed evidence of cracking and severe stress loss. The apparent high efficiency may therefore be associated with unstable flow, damage or a numerical edge effect rather than a beneficial restoration mechanism.

The efficiency map provides an initial indication of the conditions under which deformation power may be more effectively accommodated. Nevertheless, a high value of η does not necessarily indicate stable deformation. The power dissipation map must therefore be considered together with the instability criteria and the experimentally observed specimen behavior.

3.2.2. Flow-instability analysis

Flow instability was first evaluated using the instability criterion based on the extremum principles of irreversible thermodynamics. The instability parameter, ξ, is expressed as [32]:

$$\xi(\dot{\varepsilon}) = \frac{\partial \ln\left(\frac{m}{m+1}\right)}{\partial \ln(\dot{\varepsilon})} + m < 0 \tag{6}$$

where m is the strain rate sensitivity. Negative values of ξ indicate conditions under which the material is potentially susceptible to unstable flow, while $\xi = 0$ defines the boundary of the predicted instability domain.

Figure 4 presents the instability map obtained from Eq. (4) at a true strain of 0.7. The dashed boundaries define the boundary of the predicted instability domain. Three main instability domains can be identified. The first occurs at approximately 230–300 °C and strain rates between about 0.1 and 1 s^{-1}. A second domain is predicted at approximately 340–390 °C, mainly at strain rates approaching 1 s^{-1}. At these relatively high strain rates, deformation is imposed rapidly, leaving less time for thermally activated restoration processes to accommodate the accumulated strain. This may increase the tendency towards non uniform deformation, although the instability criterion alone cannot establish whether the instability takes the form of flow localization, cracking, shear band formation or microstructural heterogeneity. A third domain is observed near 200–230 °C at the lowest investigated strain rates. At these temperatures, limited dislocation mobility and restricted activation of non-basal slip systems may reduce the ability of the alloy to redistribute strain uniformly, even when deformation is applied slowly. This domain lies close to the lower boundaries of both the temperature and strain rate ranges and should therefore be interpreted cautiously, because numerical differentiation and interpolation are generally more sensitive near the edges of the experimental dataset.

In addition to the ξ criterion, flow stability was examined using the $2m/\eta$ parameter. Stable material flow is predicted when the following condition is satisfied [31, 33]:

$$\frac{2m}{\eta} > 1 \tag{7}$$

Accordingly, regions where $2m/\eta < 1$ are considered potentially susceptible to unstable deformation. Figure 5 presents the corresponding stability map at a true strain of 0.7. The most prominent unstable region is located at approximately 200–240 °C and extends over low to intermediate strain rates up to about 0.2 s^{-1}. This prediction is broadly consistent with the high flow stresses, pronounced post peak stress losses and macroscopic cracking observed at low temperatures. However, once cracking occurs, the measured decrease in stress is affected by the reduction in the effective load bearing area.

The calculated values of m, η and the instability parameters may therefore also be influenced by specimen damage in this region. A smaller unstable region is predicted at high temperatures and strain rates approaching 1 s^{-1}. Over much of the intermediate and high temperature range, particularly between approximately 320 and 400 °C at low to intermediate strain rates, $2m/\eta$ remains above unity. According to Eq. (5), these conditions are associated with comparatively stable flow. The lower flow stresses and smoother post peak responses observed in this region are consistent with improved strain accommodation, although the underlying restoration mechanisms cannot be identified from the stability map alone.

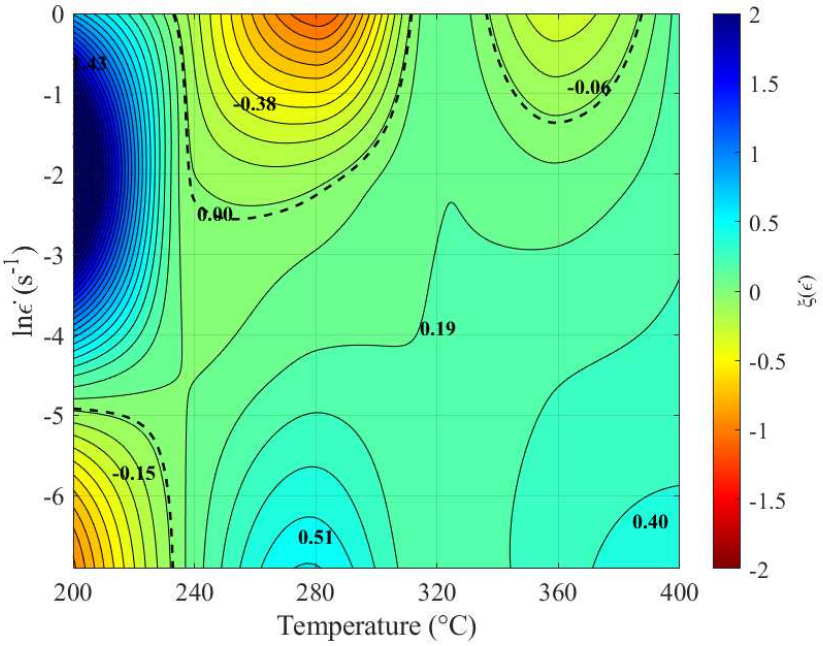


Fig. 4. Flow instability map of the extruded Mg–1Zn–0.2Ca alloy at a true strain of 0.7 based on the ξ criterion. Dashed boundaries define the boundary of the predicted instability domain.

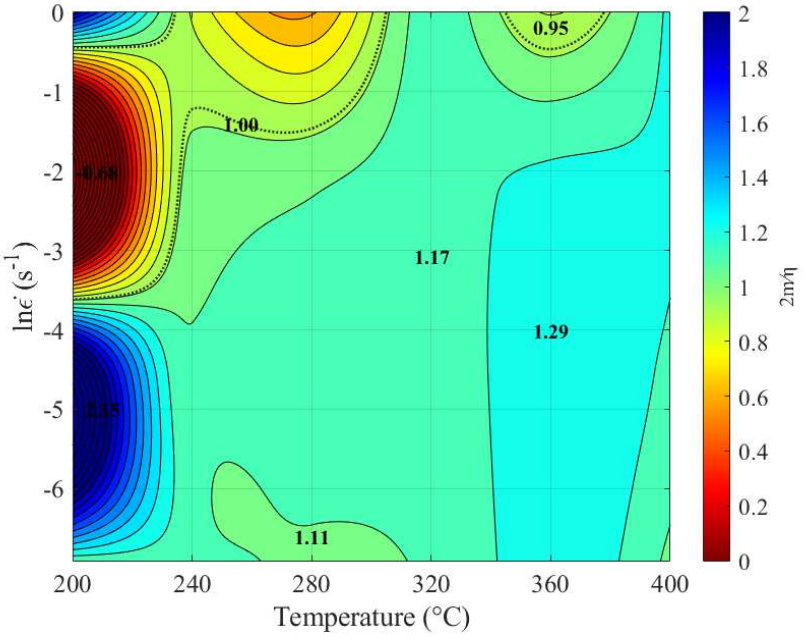


Fig. 5. Flow stability map of the extruded Mg–1Zn–0.2Ca alloy at a true strain of 0.7 based on the $2m/\eta$ criterion. Dashed boundaries define the boundary of the predicted instability domain.

The two criteria show partial, but not complete, agreement. Both indicate an increased tendency towards instability at low temperatures and at the highest strain rates, while much of the high temperature, low to intermediate strain rate region is predicted to remain comparatively stable. However, the ξ criterion identifies additional instability at approximately 230–300 °C and high strain rates, as well as at very low strain rates near 200 °C. These regions are less pronounced in the $2m/\eta$ map. The criteria should therefore be treated as complementary rather than as direct confirmation of one another. Their predicted instability boundaries are superimposed on the power dissipation efficiency map in the following section and compared with the macroscopic appearance of the compressed specimens.

3.2.3. *Processing maps and recommended deformation domain*

The processing map was constructed by superimposing the instability boundaries predicted by the ξ and $2m/\eta$ criteria onto the power dissipation efficiency map. In Fig. 6, the color contours represent the variation in η, while the dashed and dotted boundaries enclose regions predicted to be unstable according to the two criteria. The map therefore identifies conditions where relatively high-power dissipation efficiency coincides with the absence of predicted flow instability. At a true strain of 0.7, the principal high-efficiency domain is centered near 360–370 °C and a strain rate of approximately 0.005–0.01 s^{-1}, where η reaches a maximum value of about 0.46. A broader favorable deformation domain extends approximately from 340 to 380 °C and from 0.001 to 0.1 s^{-1}. Within this region, the power dissipation efficiency is generally high, reaching approximately 0.4–0.46, and the domain remains largely outside the instability boundaries predicted by both criteria.

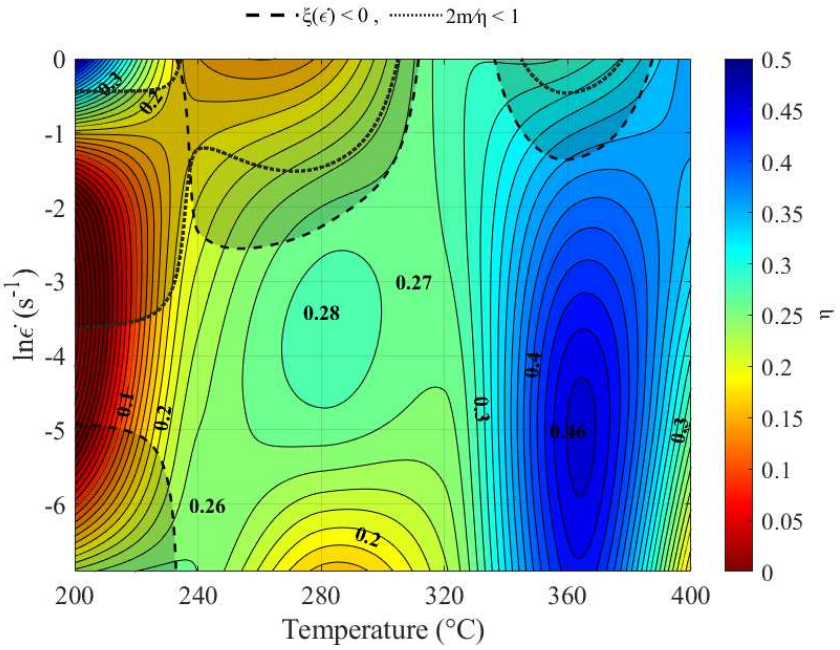


Fig. 6. Processing map of the extruded Mg–1Zn–0.2Ca alloy at a true strain of 0.7. Color contours represent the power dissipation efficiency, η, while dashed and dotted boundaries define the boundary of the predicted instability domain by the ξ and $2m/\eta$ criteria, respectively.

The high efficiency in this region indicates that, within the DMM framework, a relatively large fraction of the deformation power is associated with changes occurring within the material. Thermally activated restoration processes are likely to contribute to this response. However, the processing map alone cannot establish whether dynamic recovery or dynamic recrystallisation is dominant, nor can it demonstrate grain refinement without supporting microstructural evidence.

A secondary domain with moderate efficiency is centered at approximately 280 °C and a strain rate close to 0.02 s^{-1}, where η reaches about 0.27–0.28. More broadly, moderate values of approximately 0.25–0.30 occur between about 260 and 320 °C and strain rates of roughly 0.005–0.05 s^{-1}. Although part of this region lies outside the instability boundaries, its efficiency is lower than that of the high temperature domain, and the deformation response is likely to be more sensitive to changes in temperature and strain rate.

The region below approximately 240 °C is generally unsuitable for hot working. Although locally high values of η occur near the boundaries of the map, particularly close to 200–220 °C, these regions overlap with one or both predicted instability domains. The macroscopic cracking observed at low temperatures also indicates that the apparent high efficiency in these localised regions should not be interpreted as evidence of favorable deformation. Instability is also predicted at high strain rates, including parts of the 230–300 °C and 340–390 °C temperature ranges as the strain rate approaches 1 s^{-1}. These conditions should therefore be avoided despite the moderate or locally high values of power dissipation efficiency. Based on the map, the range of approximately 340–380 °C and 0.001–0.1 s^{-1} can be identified as the recommended deformation domain for the extruded Mg–1Zn–0.2Ca alloy at a true strain of 0.7. The highest efficiency within this domain is centered near 360–370 °C and approximately 0.005–0.01 s^{-1}. This range provides the most favorable combination of power dissipation efficiency and predicted flow stability within the conditions investigated.

The recommended window of approximately 340–380 °C and 0.001–0.1 s^{-1} is supported by high efficiency, positive and moderate m (about 0.14–0.31 at 360 °C), the absence of predicted instability across most of the region, and sound specimens. It has not, however, been validated at component scale. Forging or extrusion trials within this window, together with repeat tests, are required to confirm its processing relevance.

3.2.4. *Macroscopic assessment of the compressed specimens*

Figure 7 compares the macroscopic appearance of the specimens compressed under the 24 temperature–strain rate conditions. All specimens in Fig. 7 are shown in the same orientation and at approximately the same magnification. A clear improvement in deformability is observed with increasing temperature. Visible cracking is concentrated mainly at 200–280 °C, whereas specimens deformed at 320–400 °C generally remain macroscopically intact. At 200 °C, cracking is present at all four investigated strain rates. The specimens tested at 1, 0.1 and 0.01 s^{-1} show extensive inclined cracks and shear type damage, while a less severe but still visible crack is present at 0.001 s^{-1}. These observations indicate that deformation at 200 °C cannot be accommodated without macroscopic damage over the investigated strain rate range. This is consistent with the high flow stresses and pronounced late-stage stress losses observed in Fig. 2.

At 240 °C, the response becomes more dependent on strain rate. Clear diagonal cracks are visible in the specimens compressed at 1 and 0.1 s^{-1}, whereas those tested at 0.01 and 0.001 s^{-1} retain a comparatively regular shape without obvious macroscopic fracture. Increasing the temperature from 200 to 240 °C therefore improves deformation tolerance at the lower strain rates, although substantial damage remains at the higher rates. At 280 °C, visible cracking is mainly confined to the specimen tested at 1 s^{-1}. The specimens deformed at 0.1, 0.01 and 0.001 s^{-1} remain largely intact. This agrees with the ξ-based instability region predicted at intermediate temperatures and high strain rates and indicates that the adverse effect of rapid deformation persists at 280 °C.

At 320 °C, no obvious macroscopic cracking is visible across the investigated strain rate range. The specimens retain a more regular compressed shape than those tested at lower temperatures, suggesting a marked improvement in the ability of the alloy to accommodate deformation. On the basis of the macroscopic observations, 320 °C represents a transition from damage prone to substantially improved hot deformability. All specimens deformed at 360 and 400 °C remain macroscopically intact, including those tested at 1 s^{-1}. Their appearance supports the favorable deformation response predicted over much of the high temperature region. However, the absence of visible cracking at 360 °C and 1 s^{-1} does not agree directly with the high-strain rate instability region predicted by the ξ criterion. This difference may indicate that the predicted instability is microstructural rather than macroscopic, or that the calculated boundary is sensitive to the numerical treatment of the flow stress data.

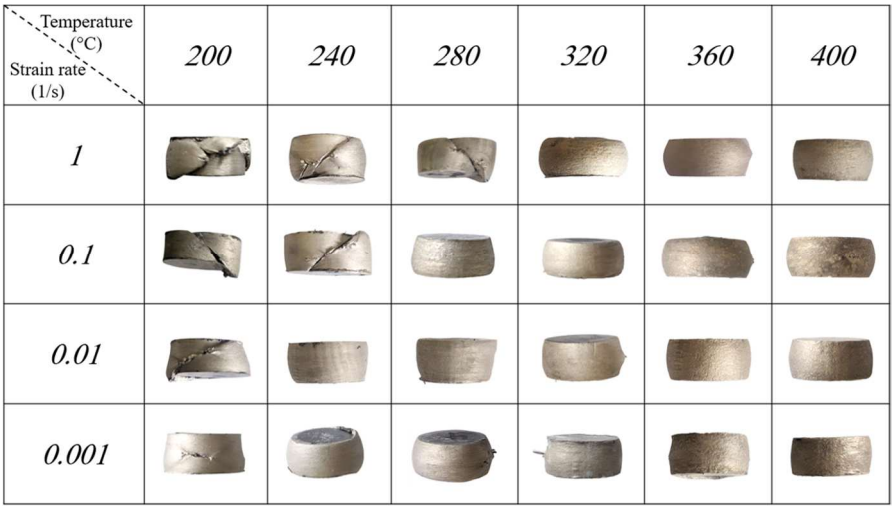


Fig. 7. Macroscopic appearance of the extruded Mg–1Zn–0.2Ca specimens after compression at temperatures of 200–400 °C and strain rates of 0.001–1 s^{-1}. Cracking is observed at all strain rates at 200 °C, at 0.1–1 s^{-1} at 240 °C, and at 1 s^{-1} at 280 °C. No obvious macroscopic cracking is visible in specimens deformed at 320–400 °C.

The specimen observations show good qualitative agreement with the principal features of the processing map. The extensive damage observed at 200 °C, the high-rate cracking at 240–280 °C and the intact specimens obtained at lower strain rates and higher temperatures support the classification of the low-temperature region as generally unfavorable. The specimens deformed at 320–400 °C show substantially improved macroscopic integrity and support the recommended high temperature processing range. Nevertheless, the agreement is not complete, particularly at 360 °C and 1 s^{-1}, and the macroscopic photographs should therefore be regarded as supporting evidence rather than complete validation of the instability predictions.

3.2.5. *Microstructural evolution*

To clarify the mechanisms behind the processing map, the microstructures at four representative conditions were examined (Fig. 8). At 200 °C and 0.001 s^{-1} (Fig. 8(a)), which lies in the instability region, a long, continuous crack runs diagonally across the specimen (arrows), and the surrounding matrix shows a heavily deformed, fine-scale structure. The inclined path of the crack is consistent with strain localization along planes of high shear when non-basal slip and dynamic restoration are limited at this temperature. The crack does not appear to follow isolated grain boundaries, and it is associated with a localized deformation zone. At 320 °C and 0.001 s^{-1} (Fig. 8(b)), which has moderate efficiency ($\eta \approx 0.23$), the microstructure consists of relatively coarse, equiaxed to irregular grains with serrated boundaries, and fine recrystallized grains are limited. This indicates that boundary migration and bulging operate at this condition, but that restoration at this temperature and strain rate is only partial. At 360 °C and 0.01 s^{-1} (Fig. 8(c)), which corresponds to the efficiency maximum ($\eta \approx 0.46$), the microstructure is much finer and more uniform than in Fig. 8(b), with fine grains distributed throughout the field of view and some residual twin-like features. This is consistent with extensive dynamic recrystallization, which dissipates a large fraction of the input power through microstructural change and gives the stable, high-efficiency response. At 360 °C and 1 s^{-1} (Fig. 8(d)), predicted to be unstable by the ξ criterion, the microstructure shows inclined bands of localized deformation (highlighted) within a fine, heterogeneous matrix. The specimen did not crack, so the predicted instability corresponds to a real microstructural change, localized flow, without macroscopic fracture.

Since the two instability criteria are not equivalent, a region may be flagged as unstable by one criterion and not by the other. In the processing maps, the union of the two unstable domains was therefore taken as the unstable region, so that a condition is regarded as unstable if either criterion predicts instability. This is a conservative choice that favors processing safety. The disagreement between the criteria has a physical basis. The ξ criterion depends on the strain-rate gradient of m and therefore detects local changes in rate sensitivity, whereas $2m/\eta$ relates the local m to the integrated efficiency and reflects the overall partitioning of power. Regions flagged by only one criterion may therefore indicate an incipient instability, rather than severe damage. The microstructures support this interpretation. At 360 °C and 1 s^{-1}, a condition flagged as unstable by the ξ criterion only, inclined bands of localized deformation are visible within a fine, heterogeneous matrix (Fig. 8(d)), although the specimen did not crack. The predicted instability therefore corresponds to an actual microstructural change, namely localized flow, which at this temperature is accommodated without fracture. The short time available for restoration at 1 s^{-1} and local deformation heating may promote this localization. In contrast, the stable conditions at 320 °C/0.001 s^{-1} and 360 °C/0.01 s^{-1} (Figs. 8(b) and (c)) show no such bands, and at 200 °C and 0.001 s^{-1} (Fig. 8(a)), in the unstable region, the localization develops into a crack. These observations justify including the single-criterion regions in the combined unstable domain. Only one region of disagreement was examined microstructurally, so this interpretation should be confirmed at further conditions.

To relate the cracking to the underlying deformation behavior, the microstructure at 200 °C and 0.001 s^{-1} is referred (Fig. 8(a)). A single continuous crack runs obliquely through the specimen, at an angle consistent with the planes of maximum shear in compression. The matrix on either side of the crack is very fine and heavily deformed, and the crack does not follow an equiaxed grain-boundary network. This is consistent with damage controlled by deformation localization: at this low temperature, limited non-basal slip and weak dynamic restoration make it difficult to accommodate the imposed strain homogeneously, so strain concentrates along narrow shear zones, where cracks nucleate and propagate. The inclined cracks on the specimens in Fig. 7 are consistent with this interpretation. At the magnification used, no distributed cavities or cracked second-phase particles were observed near the crack. The contribution of finer-scale mechanisms, such as grain-boundary separation, cracking of the Ca-containing second-phase particles, or cavitation, therefore cannot be excluded and would require higher-resolution (SEM) examination of the crack. The comparison with the other conditions indicates that localization alone does not lead to fracture. At 360 °C and 1 s^{-1} (Fig. 8(d)), localized deformation bands are visible, but the specimen remained intact, whereas at 320 and 360 °C and low strain rates (Figs. 8(b) and (c)) the microstructure is free of such bands. Cracking therefore appears when strain localization at low temperature cannot be accommodated by dynamic restoration, whereas at higher temperature the matrix can accommodate comparable localization without fracture.

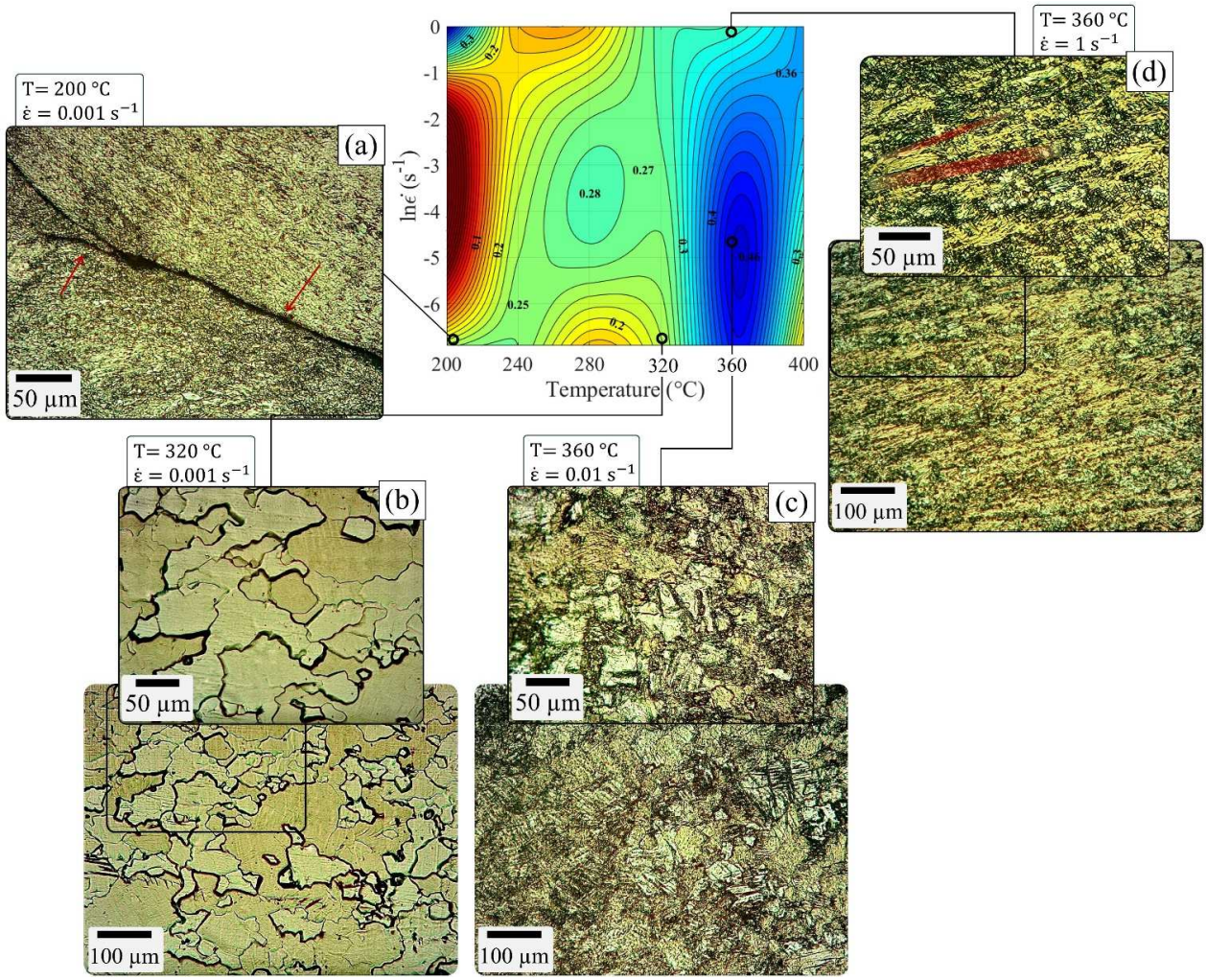
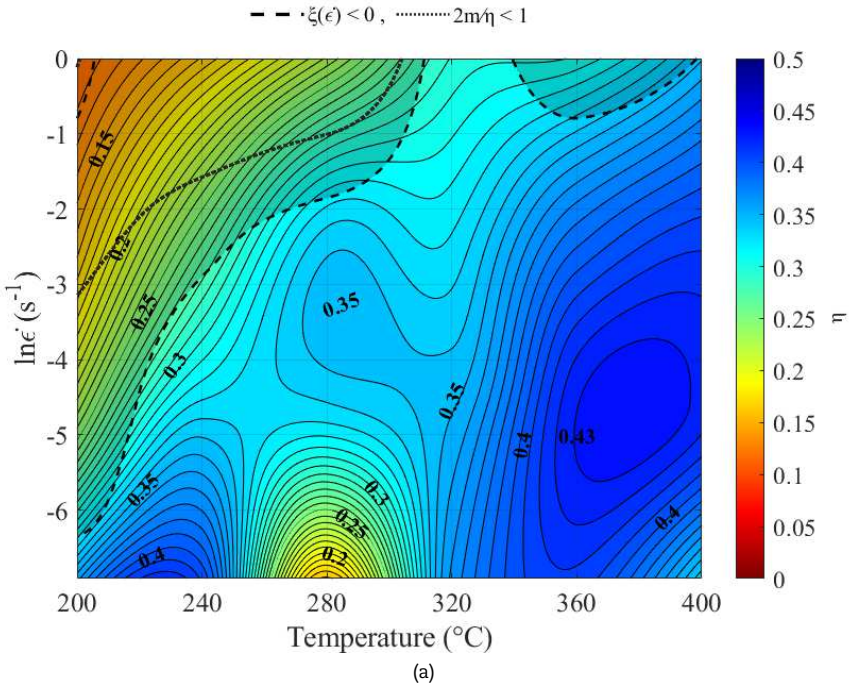
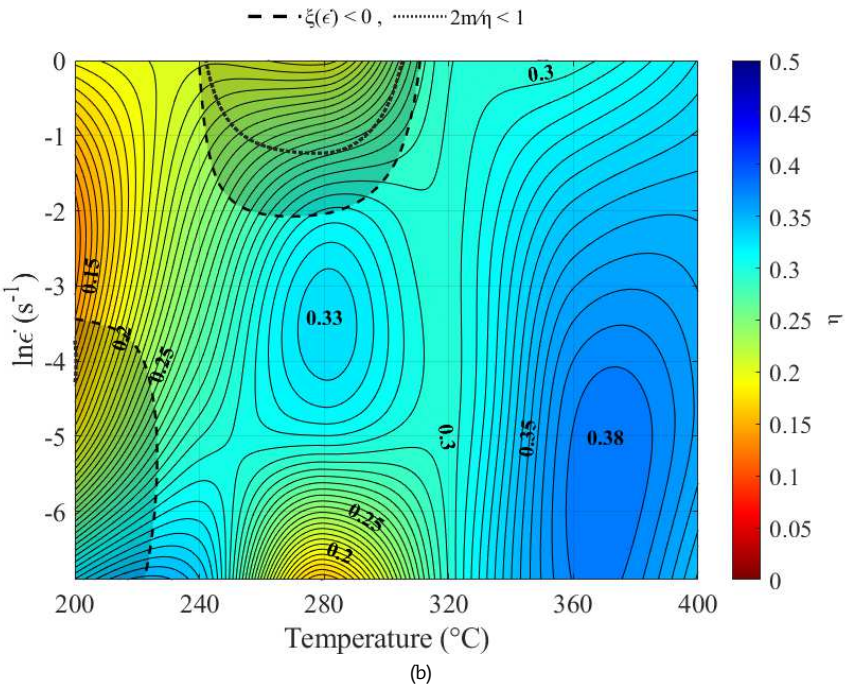


Fig. 8. Optical microstructures at selected conditions marked on the processing map: (a) 200 °C and 0.001 s^{-1} (crack indicated by arrows), (b) 320 °C and 0.001 s^{-1}, (c) 360 °C and 0.01 s^{-1}, and (d) 360 °C and 1 s^{-1} (localized deformation bands highlighted). The observations were made at the specimen center on sections parallel to the compression axis. In each panel, the smaller image is a higher-magnification view of the area outlined in the larger image.



(a)

Fig. 9. Processing maps of the extruded Mg–1Zn–0.2Ca alloy at true strains of, (a) 0.3 and (b) 0.5. Color contours represent the power dissipation efficiency, η, while dashed and dotted boundaries define the boundary of the predicted instability domain by the ξ and $2m/\eta$ criteria, respectively.



(b)

Fig. 9. Continued.

3.2.6. Evolution of the processing map with strain

To examine the effect of accumulated strain on hot workability, processing maps were constructed at true strains of 0.3 and 0.5, as shown in Fig. 9, and compared with the map obtained at a true strain of 0.7 in Fig. 6. At each strain, the instability boundaries predicted by the ξ and $2m/\eta$ criteria were superimposed on the power dissipation efficiency map. This comparison shows how both the efficiency distribution and the predicted instability domains evolve during deformation.

At a true strain of 0.3, Fig. 9(a), the principal high efficiency region is located at elevated temperatures and low to intermediate strain rates. The maximum value of η, approximately 0.43, occurs near 370–390 °C and a strain rate of about 0.005–0.01 s^{-1}. A broader favorable region extends approximately from 320 to 400 °C and from 0.001 to 0.1 s^{-1}, where relatively high efficiency coincides with the absence of extensive predicted instability. A secondary efficiency maximum of approximately 0.35 is centered near 280 °C and a strain rate of about 0.02–0.03 s^{-1}.

The instability boundaries at $\varepsilon = 0.3$ extend mainly across the low and intermediate temperature region at higher strain rates. A smaller instability domain is also predicted near 350–400 °C at strain rates approaching 1 s^{-1}. The high temperature, low strain rate region nevertheless remains largely outside the predicted instability domains and therefore represents the most favorable processing range at this stage of deformation.

At a true strain of 0.5, Fig. 9(b), the overall efficiency distribution remains similar, although the magnitude and shape of the efficiency domains change. The principal high efficiency region remains centered at approximately 360–390 °C and low strain rates, but the maximum efficiency decreases to about 0.38. A secondary domain with $\eta \approx 0.33$ is again present near 280 °C and a strain rate of approximately 0.02–0.03 s^{-1}. At $\varepsilon = 0.5$, the high-temperature, high-strain-rate instability domain visible at $\varepsilon = 0.3$ becomes less pronounced, but a broad instability region remains at approximately 240–320 °C and higher strain rates. Instability is also predicted in parts of the low-temperature region. Accumulated strain therefore changes the position and extent of the instability boundaries rather than producing a uniform improvement in stability across the entire processing space. At a true strain of 0.7, Figure 5, the high efficiency region becomes more strongly localised. The maximum efficiency increases to approximately 0.46 and is centered near 360–370 °C and a strain rate of about 0.005–0.01 s^{-1}. A broader favorable domain remains between approximately 340 and 380 °C and strain rates of 0.001–0.1 s^{-1}. However, instability is again predicted at high strain rates over parts of the intermediate and high temperature ranges, as well as within the low-temperature region.

The comparison of the three maps shows that the strain dependence of the processing response is not monotonic. The maximum efficiency decreases from approximately 0.43 at $\varepsilon = 0.3$ to 0.38 at $\varepsilon = 0.5$, before increasing to approximately 0.46 at $\varepsilon = 0.7$. Similarly, the instability domains shift, contract or reappear as strain increases. These changes reflect the evolving flow response of the alloy, but they cannot be assigned specifically to dynamic recovery, dynamic recrystallisation or damage without supporting microstructural evidence. Despite these strain dependent variations, all three maps identify the high temperature, low to intermediate strain rate region as the most consistently favorable deformation range. The common recommended domain can therefore be placed at approximately 340–380 °C and 0.001–0.1 s^{-1}. Within this range, relatively high-power dissipation efficiency generally coincides with the absence of extensive instability predicted by either criterion. In contrast, temperatures below approximately 240 °C remain unfavorable over much of the investigated strain rate range, while conditions approaching 1 s^{-1} show an increased tendency towards instability at several temperatures. The temperature and strain rate determine the general location of the favorable processing domain, whereas accumulated strain affects the magnitude of the power dissipation efficiency and the shape and extent of the predicted instability boundaries.

4. Conclusions

The hot deformation behavior of an extruded Mg–1Zn–0.2Ca alloy was investigated by isothermal compression at 200–400 °C and 0.001–1 s^{-1}, and processing maps were constructed at true strains of 0.3, 0.5 and 0.7. The main conclusions are as follows:

– The flow stress decreased with increasing temperature and increased with increasing strain rate. Abrupt late-stage stress losses at low temperatures were associated, at least partly, with specimen cracking.

- At a true strain of 0.7, the maximum power dissipation efficiency of about 0.46 occurred at 360–370 °C and 0.005–0.01 s^{-1}, within a broader stable domain at approximately 340–380 °C and 0.001–0.1 s^{-1}. The maps evolved non-monotonically with strain, with the maximum efficiency changing from about 0.43 ($\varepsilon = 0.3$) to 0.38 ($\varepsilon = 0.5$) and 0.46 ($\varepsilon = 0.7$).
- The ξ and $2m/\eta$ instability criteria agreed only partially, and the union of their unstable regions was used for a conservative assessment. Both indicated instability at low temperatures and at strain rates approaching 1 s^{-1}, whereas the ξ criterion alone predicted additional instability, such as at 360 °C and 1 s^{-1}.
- Cracking occurred at 200 °C under all strain rates, at 240 °C under 0.1–1 s^{-1}, and at 280 °C under 1 s^{-1}, but not at 320–400 °C. Microstructural observations indicated that the crack at 200 °C followed an inclined path of localized deformation. At 360 °C and 1 s^{-1} localized deformation bands formed without cracking, so the instability predicted there corresponds to incipient localized flow and not to fracture.
- Approximately 340–380 °C and 0.001–0.1 s^{-1} is recommended for hot deformation of the alloy, whereas conditions below about 240 °C and those approaching 1 s^{-1} should be avoided. Since each condition was tested once and the window has not been validated at component scale, repeat tests and processing trials are recommended.

Author Contributions

M. Kamrava contributed to the Investigation, Writing original draft. A. Najafi contributed to the Investigation, Y. Mazaheri contributed to the Methodology. E. Bagherpour contributed to the Formal analysis. M. Reihanian contributed to the Methodology, Writing-review and editing. R.Z. Valiev contributed to the Methodology. R. Ebrahimi contributed to the Supervision, Conceptualization, Methodology, Writing-review and editing. The manuscript was written through the contribution of all authors. All authors discussed the results, reviewed, and approved the final version of the manuscript.

Acknowledgment

Not applicable.

Conflict of Interest

The authors declare that they have no known competing financial interests or personal relationships that could have appeared to influence the work reported in this paper.

Funding

This work is based upon research funded by Iran National Science Foundation (INSF) under project No.4021954 and Russian Science Foundation (RSF) under project No. 24-43-20015. E. Bagherpour would like to acknowledge the use of the BCAST physical thermomechanical simulation lab, set up through the funding received from Research England UKRI grant: entitled “Future Metallurgy Centre”.

Data Availability Statements

The raw/processed data required to reproduce these findings can be shared upon request.

References

[1] Han, H.-S., Loffredo, S., Jun, I., Edwards, J., Kim, Y.-C., Seok, H.-K., Witte, F., Mantovani, D., Glyn-Jones, S., Current status and outlook on the clinical translation of biodegradable metals, *Materials Today*, 23, 2019, 57–71.
[2] Zheng, Y.F., Gu, X.N., Witte, F., Biodegradable metals, *Materials Science and Engineering: R: Reports*, 77, 2014, 1–34.
[3] Vinogradov, A., Merson, E., Myagkikh, P., Linderov, M., Brilevsky, A., Merson, D., Attaining high functional performance in biodegradable Mg-alloys: an overview of challenges and prospects for the Mg-Zn-Ca system, *Materials*, 16(3), 2023, 1324.
[4] Roh, H.-J., Park, J., Lee, S.-H., Kim, D.-H., Lee, G.-C., Jeon, H., Chae, M., Lee, K.-S., Sun, J.-Y., Lee, D.-H., Optimization of the clinically approved Mg-Zn alloy system through the addition of Ca, *Biomaterials Research*, 26(1), 2022, 41.
[5] Pulido-González, N., Torres, B., García-Rodríguez, S., Rodrigo, P., Bonache, V., Hidalgo-Manrique, P., Mohedano, M., Rams, J., Mg–1Zn–1Ca alloy for biomedical applications. Influence of the secondary phases on the mechanical and corrosion behaviour, *Journal of Alloys and Compounds*, 831, 2020, 154735.
[6] Lu, Y., Bradshaw, A., Chiu, Y.-L., Jones, I., Effects of secondary phase and grain size on the corrosion of biodegradable Mg–Zn–Ca alloys, *Materials Science and Engineering: C*, 48, 2015, 480–486.
[7] Wang, H., Jia, W., Ma, L., Huang, Z., Zhang, J., Ning, F., Lei, J., Fracture behavior of AZ31 magnesium alloy under continuously variable stress triaxiality, *Engineering Failure Analysis*, 169, 2025, 109177.
[8] Jaimin, A., Kotkunde, N., Singh, S.K., Suresh, K., Damage models for forming limit prediction of AZ31B alloy: An experimental and simulation-based approach, *Engineering Failure Analysis*, 170, 2025, 109314.
[9] Wang, X., Zhang, H., Dong, X., A ductile fracture model for AZ31B considering current parameters in electrically-assisted forming process, *Engineering Failure Analysis*, 129, 2021, 105681.
[10] Zhang, B., Wang, Y., Geng, L., Lu, C., Effects of calcium on texture and mechanical properties of hot-extruded Mg–Zn–Ca alloys, *Materials Science and Engineering: A*, 539, 2012, 56–60.
[11] Ma, D., Yuan, S., Luan, S., Jin, P., Hu, H., Wang, J., Li, X., Hot deformation behavior, microstructure evolution and slip system of Mg-2Zn-0.5 Mn-0.2 Ca alloy, *Journal of Materials Research and Technology*, 21, 2022, 1643–1654.
[12] Shah, S., Liu, M., Khan, A., Ahmad, F., Chaudry, U.M., Khan, M.Y., Abdullah, M., Xu, S., Peng, Z., Recrystallization aspects and factors affecting their roles in Mg alloys: A comprehensive review, *Journal of Magnesium and Alloys*, 13(5), 2025, 1879–1914.
[13] Rao, K.P., Prasad, Y.V.R.K., Dharmendra, C., Suresh, K., Hort, N., Dieringa, H., Review on Hot Working Behavior and Strength of Calcium-Containing Magnesium Alloys, *Advanced Engineering Materials*, 20(9), 2018, 1701102.
[14] Rao, K.P., Suresh, K., Prasad, Y.V.R.K., Dharmendra, C., Hort, N., Dieringa, H., High temperature strength and hot working technology for as-cast Mg–1Zn–1Ca (ZX11) alloy, *Metals*, 7(10), 2017, 405.
[15] Hradilová, M., Montheillet, F., Fraczkiewicz, A., Desrayaud, C., Lejcek, P., Effect of Ca-addition on dynamic recrystallization of Mg–Zn alloy during hot deformation, *Materials Science and Engineering: A*, 580, 2013, 217–226.
[16] Papillon, J., Salero, P., Mercier, F., Fabrègue, D., Maire, É., Compressive deformation behavior of dendritic Mg–Ca (–Zn) alloys at high temperature, *Materials Science and Engineering: A*, 763, 2019, 138180.
[17] Zareian, Z., Emamy, M., Malekan, M., Mirzadeh, H., Kim, W., Bahmani, A., Tailoring the mechanical properties of Mg–Zn magnesium alloy by calcium addition and hot extrusion process, *Materials Science and Engineering: A*, 774, 2020, 138929.

[18] Zheng, H., Yu, L., Lyu, S., You, C., Chen, M., Insight into the role and mechanism of nano MgO on the hot compressive deformation behavior of Mg-Zn-Ca alloys, *Metals*, 10(10), 2020, 1357.
[19] Najafi, A., Reihanian, M., Bagherpour, E., Mendis, C., Mazaheri, Y., Botkin, A., Valiev, R., Ebrahimi, R., Tailoring microstructure and mechanical behavior of Mg-1Zn-0.2 Ca alloy through Hot Extrusion with a Cosine-Profile Die, *Materials Today Communications*, 49, 2025, 113832.
[20] Razavi, S.A., Mirabdolazimi, N., Ebrahimi, R., Modeling Static Recrystallization during Non-Isothermal Heating in Biomedical Mg-1Zn-0.2 Ca Magnesium Alloy Based on Isothermal Kinetic Data, *Results in Engineering*, 28, 2025, 107663.
[21] Mirabdolazimi, N., Reihanian, M., Bagherpour, E., Mendis, C., Rezvani, A., Valiev, R., Ebrahimi, R., Annealing-induced hardening in an ultrafine-grained Mg–Zn–Ca alloy processed by high pressure torsion, *Journal of Materials Research and Technology*, 42, 2026, 6742-6755.
[22] Prasad, Y., Gegel, H., Doraivelu, S., Malas, J., Morgan, J., Lark, K., Barker, D., Modeling of dynamic material behavior in hot deformation: Forging of Ti-6242, *Metallurgical Transactions A*, 15(10), 1984, 1883–1892.
[23] Prasad, Y., Seshacharyulu, T., Modelling of hot deformation for microstructural control, *International Materials Reviews*, 43(6), 1998, 243–258.
[24] Jedrasiak, P., Shercliff, H., Finite element analysis of small-scale hot compression testing, *Journal of Materials Science & Technology*, 76, 2021, 174–188.
[25] Li, Y., Onodera, E., Matsumoto, H., Yamanaka, K. Chiba, A., Compensation for friction and temperature increase due to adiabatic heating during hot compression testing and construction of a processing map of biomedical Co–29Cr–6Mo–0.16N alloy, *Journal of the Japan Society for Technology of Plasticity*, 51(590), 2010, 221–226.
[26] Qin, Y.-J., Pan, Q.-L., He, Y.-B., Li, W.-B., Liu, X.-Y., Fan, X., Modeling of flow stress for magnesium alloy during hot deformation, *Materials Science and Engineering: A*, 527(10-11), 2010, 2790–2797.
[27] Wu, G.-C., Lin, Y., Zhou, Y., Long, J.-C., He, D.-G., Interphase boundary engineering for microstructure control and processing optimization in hot working of dual-phase Ti alloys, *Materials Science and Engineering: A*, 2026, 150838.
[28] Zhang, S., Lin, Y., Ling, Y.-H., He, D.-G., Chen, M.-S., Wan, M., Wu, G.-C., Zeng, N.-F., Zhang, H.-J., Naseri, M., Modeling flow behaviors and microstructure evolution of Ti55511 alloy during the double-stage hot deformation process utilizing machine learning algorithm, *Metals and Materials International*, 32(3), 2026, 874–894.
[29] Chen, Z.-J., Lin, Y., Zhang, S., Zhu, J.-C., Zeng, N.-F., Wu, G.-C., Yang, Q.-M., A continuum-field-enabled multiscale framework coupling crystal plasticity and cellular automaton for discontinuous dynamic recrystallization: Application to a nickel-based superalloy, *Journal of Alloys and Compounds*, 2026, 188264.
[30] Eskandari, H., Reihanian, M., Alavi Zaree, S., An analysis of efficiency parameter and its modifications utilized for development of processing maps, *Iranian Journal of Materials Forming*, 10(4), 2023, 45–51.
[31] Ebrahimi, R., Najafizadeh, A., Optimization of hot workability in ti-if steel by using the processing map, *International Journal of ISSI*, 1(1), 2004, 1–7.
[32] Murty, S.N., Rao, B.N., On the development of instability criteria during hotworking with reference to IN 718, *Materials Science and Engineering: A*, 254(1-2), 1998, 76–82.
[33] Narayana Murty, S., Nageswara Rao, B., Kashyap, B., Instability criteria for hot deformation of materials, *International Materials Reviews*, 45(1), 2000, 15–26.

ORCID iD

M. Kamrava https://orcid.org/0009-0001-8121-9711
A. Najafi https://orcid.org/0009-0001-7734-8721
Y. Mazaheri https://orcid.org/0000-0002-9478-1252
E. Bagherpour https://orcid.org/0000-0002-7405-1949
M. Reihanian https://orcid.org/0000-0003-4618-5509
R.Z. Valiev https://orcid.org/0000-0003-4340-4067
R. Ebrahimi https://orcid.org/0000-0001-8057-5733

© 2026 Shahid Chamran University of Ahvaz, Ahvaz, Iran. This article is an open access article distributed under the terms and conditions of the Creative Commons Attribution-NonCommercial 4.0 International (CC BY-NC 4.0 license) (http://creativecommons.org/licenses/by-nc/4.0/).

How to cite this article: Kamrava M., et al. Hot Deformation Behavior and Processing Map Development for Biodegradable Mg–1Zn–0.2Ca Alloy, *J. Appl. Comput. Mech.*, xx(x), 2026, 1–13. https://doi.org/10.22055/jacm.2026.49819.6267

Publisher's Note Shahid Chamran University of Ahvaz remains neutral with regard to jurisdictional claims in published maps and institutional affiliations.